

High Energy Afterglow Emission from Gamma-Ray Bursts

Yi-Zhong Fan^{1,2,4*}, Tsvi Piran¹ †, Ramesh Narayan³ ‡ and Da-Ming Wei² §

¹The Racah Inst. of Physics, Hebrew University, Jerusalem 91904, Israel

²Purple Mountain Observatory, Chinese Academy of Science, Nanjing 210008, China

³Institute for Theory and Computation, Center for Astrophysics, Harvard University, 60 Garden St., Cambridge, MA, 02138

⁴Neils Bohr International Academy, Niels Bohr Institute, University of Copenhagen, Blegdamsvej 17, 2100 Copenhagen, Denmark

Accepted Received; in original form

ABSTRACT

We calculate the very high energy (sub-GeV to TeV) inverse Compton emission of GRB afterglows. We argue that this emission provides a powerful test of the currently accepted afterglow model. We focus on two processes: synchrotron self-Compton (SSC) emission within the afterglow blast wave, and external inverse Compton (EIC) emission which occurs when flare photons (produced by an internal process) pass through the blast wave. We show that if our current interpretations of the Swift XRT data are correct, there should be a canonical high energy afterglow emission light curve. Our predictions can be tested with high energy observatories such as GLAST, Whipple, H.E.S.S., MAGIC and Kangaroo. Under favorable conditions we expect afterglow detections in all these detectors.

Key words: Gamma Rays: bursts—ISM: jets and outflows—radiation mechanisms: nonthermal

1 INTRODUCTION

EGRET detected more than 30 Gamma-Ray Bursts (GRBs) with GeV emission (Schneid et al. 1992; Sommer et al. 1994; Hurley et al. 1994; Schaefer et al. 1998; González et al. 2003). The highest energy photon detected was the 18 GeV photon which arrived 4500 seconds after the trigger of GRB 940217 (Hurley et al. 1994). These observations motivated many interesting ideas. Some focused on prompt high energy photon emission, e.g., synchrotron-self-Compton (SSC) emission or inverse Compton scattering of photons emitted by one shell by electrons in another shell (Takagi & Kobayashi 2005). Others focused on high energy afterglow processes: the interaction of ultra-relativistic protons with a dense cloud (Katz 1994), SSC in early forward and reverse shocks (Mészáros & Rees 1994), electromagnetic cascade of TeV γ -rays in the infrared/microwave background (Plaga 1995), synchrotron radiation of ultra-high energy forward shock protons (Totani 1998), and inverse Compton scattering of prompt γ -rays by reverse shock electrons (Beloborodov 2005).

Two kinds of high energy afterglow emission models have been discussed extensively. The first is SSC emission. Motivated by the successful detection of an optical flash in GRB 990123 (Akerlof et al. 1999; Sari & Piran 1999;

Mészáros & Rees 1999), Wang, Dai & Lu (2001a, b), Pe’er & Waxman (2005) and Kobayashi et al. (2007) calculated SSC emission from the reverse shock. Granot & Guetta (2003) and Pe’er & Waxman (2004) applied these ideas to GRB 941017. The high energy SSC component of the forward component was calculated by Dermer, Chiang & Mitman (2000), Sari & Esin (2001), and Zhang & Mészáros (2001b). The second family of models involves the external inverse Compton (EIC) process. These include Comptonization of the prompt photons by the forward shock electrons (Fan, Zhang & Wei 2005b), and upscattering of far-UV/X-ray flare photons (assuming that they originate in internal shocks) by the forward shock (Wang, Li & Mészáros 2006; Fan & Piran 2006b).

Most of the above calculations were based on the standard afterglow model. However, recently, *Swift* has detected numerous GRBs whose early (first 10^4 s) afterglow emission cannot be reproduced within the standard model (Mészáros 2006; Piran & Fan 2007; Zhang 2007). Various modifications of the standard model have been put forward to explain the observations. However, none are compelling and the validity of the whole model is now in question.

High energy emission provides a new window into afterglow physics and can provide an independent test of models. Motivated by this, we calculate the predicted high energy afterglow emission in different scenarios. We show that there is a canonical high energy GRB afterglow light curve which ought to be observed (see Fig. 15). The detection of the predicted high energy emission features by observations

* Golda Meir Fellow, E-mail: yzfan@pmo.ac.cn

† tsvi@phys.huji.ac.il

‡ narayan@cfa.harvard.edu

§ dmwei@pmo.ac.cn

with GLAST or ground-based gamma-ray detectors would enable us to test the validity of the overall model as well as the specific modifications that have been put forward to explain *Swift* observations.

The paper is structured as follows. In section 2 we review *Swift* GRB afterglow observations and their interpretation. In section 3 we describe the methods we employ for careful calculations of the inverse Compton effect; this section may be skipped if one is interested only in the results. In section 4 we calculate the SSC emission of the forward shock, and in section 5 we calculate the possible high energy emission associated with X-ray flares, including both SSC emission from within the flare and EIC emission from the forward shock. In section 6 we discuss the prospects for detecting high energy afterglows by GLAST and ground-based telescopes. We conclude in section 7 with a summary.

2 SWIFT GRB AFTERGLOW OBSERVATIONS

In the pre-*Swift* era, most of the afterglow data was collected hours after the GRB. These data were found to be consistent with the external forward shock model, though sometimes energy injection, a wind profile, or structured or patchy jets had to be invoked to account for the observations (Piran 2004). The *Swift* satellite has changed the situation. The X-ray Telescope (XRT) and the UV/optical Telescope (UVOT) onboard this satellite can slew to the direction of a GRB in real time and record the early broad band afterglow light curves. A schematic X-ray afterglow light curve based on the XRT data has been summarized by Zhang et al. (2006) and Nousek et al. (2006) (see Fig. 1) and consists of the following features: A very early sharp decline (phase-I); A shallow decline of the X-ray afterglow (phase-II); A “normal” decay phase (phase-III), possibly followed by a jet break (phase-IV); Energetic X-ray flares (phase-V), which may show up during any phase. Note that not all of these features have been detected in every burst. We focus here on the most remarkable of the new features: the slow decline (phase-II) and the flares (phase-V). Both are expected to have associated signatures in the high energy emission.

In about half of the *Swift* GRBs, the X-ray lightcurves show an extended flattening (phase-II). In most cases, but not all, there is no change in the spectral slope when the light curve makes a transition from the shallow phase-II segment to the “normal” phase-III segment. The usual interpretation of the shallow phase is that it involves energy injection into the blast wave (Zhang et al. 2006; Nousek et al. 2006; Granot & Kumar 2006). An alternative possibility is that the parameter ϵ_e , which measures the fraction of shock energy transferred to the downstream electrons, varies with time¹, as would be the case if this parameter is shock-strength dependent. In either case the corresponding SSC emission of the forward shock would be different from the one anticipated in the standard afterglow model, as well as from each other.

¹ Note, however, that for some GRBs the break in the X-ray light curve is not accompanied by a break in the optical light curve (see Figure 1). The interpretation of this chromatic behavior is less clear. In the present work, we focus on the cases in which the X-ray and optical light curves break achromatically.

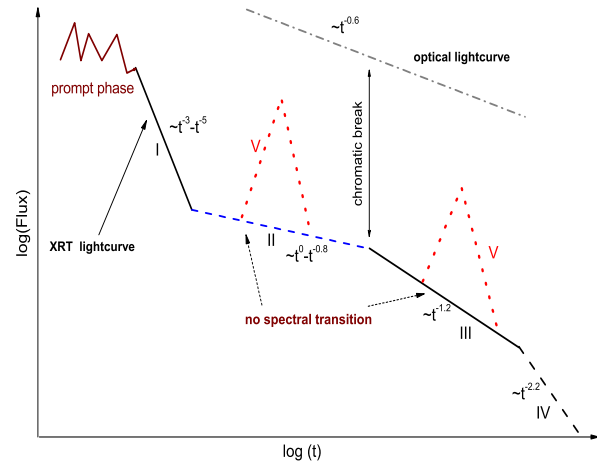


Figure 1. Schematic cartoon of the X-ray light curve of a GRB and its afterglow, based on *Swift* XRT data (see Zhang et al. 2006 and Nousek et al. 2006 for similar plots). Also shown is a schematic optical light curve, which often does not show the same breaks as the X-ray light curve (Fan & Piran 2006a; Panaitescu et al. 2006; Huang et al. 2007).

Energetic X-ray flares (phase-V) have been detected in several pre-*Swift* GRBs and in about half the *Swift* GRBs (Piro et al. 2005; Burrows et al. 2005; Galli & Piro 2006; Chincarini et al. 2007). The rapid decline of the flares suggests that they arise due to “late internal shocks” resulting from reactivation of the central engine (Fan & Wei 2005; Zhang et al. 2006; Fan et al. 2005a; King et al. 2005; Nousek et al. 2006; Falcone et al. 2006; Perna et al. 2006; Proga & Zhang 2006; Zou, Dai & Xu 2006; Wu et al. 2007; Dai et al. 2006; Gao & Fan 2006; Lazzati & Perna 2007; Krimm et al. 2007; Chincarini et al. 2007). An alternative interpretation is that the X-ray flares arise due to refreshed shocks (Piro et al. 2005; Galli & Piro 2006; Wu et al. 2007; Guetta et al. 2007). Once again, the GeV emission can serve to distinguish between the models.

If the flares are produced by internal shocks, most of the up-scattered photons would arrive after the far-UV/X-ray flare. The high energy photons in this scenario will be produced by scattering of the flare photons in the external shock. In the EIC process, the duration of the high energy emission is stretched by the spherical curvature of the blast wave (Beloborodov 2005; Wang et al. 2006; Fan & Piran 2006b) and is further extended by the highly anisotropic distribution of the up-scattered photons (Fan & Piran 2006b; see our Fig.12 for a comparison). For the latter effect, see Aharonian & Atoyan (1981), Ghisellini et al. (1991) and Brunetti (2001) for details.

3 SELF CONSISTENT COMPUTATION OF INVERSE COMPTON SCATTERING WITH KLEIN-NISHINA SUPPRESSION

The relativistic electrons that are present in any synchrotron source will also produce very high energy photons via inverse Compton scattering (either SSC or EIC). We turn now to

a calculation of this emission. When the energy of the electrons and the seed photons is sufficiently large it is necessary to take into account the Klein-Nishina correction to the scattering cross section. We also need to include the inverse Compton cooling in calculating the energy distribution of the relativistic electrons.

The essential problem is to calculate carefully the Compton parameter, Y , the ratio between the power loss through inverse Compton scattering and synchrotron radiation ($P'_{\text{ic}}(\gamma_e)$ and $P'_s(\gamma_e)$ respectively):

$$Y(\gamma_e) \equiv P'_{\text{ic}}(\gamma_e)/P'_s(\gamma_e). \quad (1)$$

Throughout this work, the superscript ' indicates that the quantity is measured in the rest frame of the emitting region. In the regime of Thomson scattering, Y is a constant, independent of the electron Lorentz factor γ_e , and one obtains a constant reduction in the amplitude of the synchrotron emission compared to the case with no inverse Compton scattering. This makes computations relatively easy. However, in the general case, since the Klein-Nishina correction to Y depends on γ_e , the effect of inverse Compton scattering on the spectrum and on the electron energy distribution is non-trivial.

The power emitted in synchrotron radiation by an electron with Lorentz factor γ_e is:

$$P'_s(\gamma_e) = (\gamma_e^2 - 1)\sigma_T B'^2 c / (6\pi), \quad (2)$$

where B' is the strength of the magnetic field. The corresponding spectral energy distribution of the radiation is

$$P'_s(\nu', \gamma_e) d\nu' = P'_s(\gamma_e) F \left[\frac{\nu'}{\nu'_s(\gamma_e)} \right] \frac{d\nu'}{\nu'_s(\gamma_e)}, \quad (3)$$

where $\nu'_s(\gamma_e) = 3\gamma_e^2 e B' / (4\pi m_e c)$,

$$F(x) = x \int_x^\infty K_{5/3}(\zeta) d\zeta, \quad (4)$$

and $K_{5/3}(\zeta)$ is the modified Bessel function.

The power emitted via inverse Compton scattering is given by:

$$P'_{\text{ic}}(\gamma_e) = \int_0^\infty h\nu'_{\text{ic}} \frac{dN'_\gamma}{dt d\nu'_{\text{ic}}} d\nu'_{\text{ic}}, \quad (5)$$

where ν'_{ic} is the frequency of the photon after scattering. The quantity $dN'_\gamma/dt d\nu'_{\text{ic}}$ is the scattered photon spectrum per electron (Blumenthal & Gould 1970). It is related to the spectral energy distribution of the inverse Compton radiation emitted by an electron:

$$P'_{\text{ic}}(\nu'_{\text{ic}}, \gamma_e) d\nu'_{\text{ic}} = h\nu'_{\text{ic}} \frac{dN'_\gamma}{dt d\nu'_{\text{ic}}} d\nu'_{\text{ic}}. \quad (6)$$

We define the auxiliary quantities $g \equiv \gamma_e h\nu' / (m_e c^2)$, $f \equiv h\nu'_{\text{ic}} / (\gamma_e m_e c^2)$ and $q \equiv f / [4g(1-f)]$, where $h\nu$ is the photon energy before scattering. The factor g determines the regime of scattering, with the Thomson limit corresponding to $g \ll 1$. The factor f satisfies $h\nu' / (\gamma_e m_e c^2) \leq f \leq 4g / (1+4g)$ (Jones 1968; Blumenthal & Gould 1970). We can express $dN'_\gamma/dt d\nu'_{\text{ic}}$ in terms of these quantities and in terms of the frequency distribution of the seed photons $n_{\nu'}$:

$$\frac{dN'_\gamma}{dt d\nu'_{\text{ic}}} = \frac{3\sigma_T c n_{\nu'} d\nu'}{4\gamma_e^2 \nu'} [2q \ln q + (1+2q)(1-q)]$$

$$+ \frac{1}{2} \frac{(4gq)^2}{1+4gq} (1-q)]. \quad (7)$$

To complete the calculation we need to know the frequency distribution of seed photons $n_{\nu'}$. For EIC this is simple since the photons originate from an external source. For SSC, however, the situation is more complicated. This is because the photons are produced via synchrotron emission by the same electrons that are participating in inverse Compton scattering. The additional cooling of these electrons by IC influences their energy distribution and thus their synchrotron emission. We have solved this problem by two different approaches. First, we have used a simple ‘‘instantaneous’’ approach which involves a single integral equation. This method, which we describe in section 3.1, is conceptually simple and computationally fast. It is, however, approximate. We then describe in section 3.2 a more detailed and general dynamical approach. This more accurate method is the one we have used for all the calculations presented later in this paper. However, the two methods give very similar results in a very wide energy range, as seen in Fig.2.

3.1 Instantaneous approximation

In this approach we assume a functional form for the electron energy distribution $n(\gamma_e)$ produced through acceleration in the shock front, and consider its instantaneous modification due to cooling. An electron of Lorentz factor γ_e has a cooling time given by

$$t'_c(\gamma_e) = \frac{\gamma_e m_e c^2}{P'_s(\gamma_e) + P'_{\text{ic}}(\gamma_e)}. \quad (8)$$

If $t'_c(\gamma_e)$ is longer than the dynamical time $t'_d \sim R/\Gamma c$, where R is the radius of the shock front relative to the central engine and Γ is the bulk Lorentz factor of the outflow, then the electron produces synchrotron and IC emission for the entire time t'_d . However, when $t'_c(\gamma_e)$ is shorter than t'_d , the electron radiates only for a time $t'_c(\gamma_e)$. Thus, the total spectral radiation density produced by all the electrons in the fluid is given by

$$U_{\nu'} \equiv n_{\nu'} h\nu' = \int_{\gamma_{e,\min}}^\infty [P'_s(\nu', \gamma_e) + P'_{\text{ic}}(\nu', \gamma_e)] \times \text{Min}[t'_d, t'_c(\gamma_e)] n(\gamma_e) d\gamma_e, \quad (9)$$

The spectral power distributions $P'_s(\nu', \gamma_e)$ and $P'_{\text{ic}}(\nu', \gamma_e)$ are calculated as described earlier. For the inverse Compton power, we write eq. (6) as $P'_{\text{ic}}(\nu'_{\text{ic}}, \gamma_e) d\nu'_{\text{ic}} \approx (1+g)cU_{\nu'} \sigma(\nu', \gamma_e) d\nu'_{\text{ic}}$, where $\sigma(\nu', \gamma_e)$ is the Klein-Nishina cross-section, which is equal to

$$\sigma(\nu', \gamma_e) = \frac{3}{4} \sigma_T \left\{ \frac{(1+g)}{g^3} \left[\frac{2g(1+g)}{(1+2g)} - \ln(1+2g) \right] + \frac{1}{2g} \ln(1+2g) - \frac{(1+3g)}{(1+2g)^2} \right\}. \quad (10)$$

Equation (9) is an integral equation, since the function $P'_{\text{ic}}(\nu', \gamma_e)$ inside the integral itself depends on $U_{\nu'}$. The quantity $\gamma_{e,\min}$ is the smallest γ_e down to which electrons are present. In dealing with equation (9) we need to consider two cases (see Sari, Piran & Narayan 1998 for details and for the definitions of quantities):

Slow Cooling: In this case, electrons with $\gamma_e = \gamma_m$ have a cooling time $t'_c(\gamma_m) > t'_d$. Then, $\gamma_{e,\min} = \gamma_m$, and we may use equation (9) directly with $\gamma_{e,\min} = \gamma_m$ and $n(\gamma_e)$ given by the original energy distribution produced in the shock.

Fast Cooling: Here, all electrons with $\gamma_e \geq \gamma_m$ have $t'_c(\gamma_e) < t'_d$. Therefore, electrons will continue to cool below γ_m to a minimum $\gamma_{e,\min}$ such that

$$t'_c(\gamma_{e,\min}) = t'_d. \quad (11)$$

Now, for the range $\gamma_{e,\min} \leq \gamma_e < \gamma_m$, all the electrons are available for radiating. Initially, most of the electrons are at γ_m , and as these electrons cool each electron will pass every γ_e between γ_m and $\gamma_{e,\min}$ (where all these electrons accumulate). Hence we have

$$n(\gamma_e) \sim n(\gamma_m), \quad \gamma_{e,\min} \leq \gamma_e < \gamma_m. \quad (12)$$

As usual, we assume a power-law distribution for the electron Lorentz factor:

$$n(\gamma_e)d\gamma_e \propto \gamma_e^{-p}d\gamma_e, \quad \gamma_e \geq \gamma_m, \quad (13)$$

for which γ_m is given by (Sari et al. 1998)

$$\gamma_m = \epsilon_e \left(\frac{p-2}{p-1} \right) \frac{m_p}{m_e} (\Gamma - 1) + 1. \quad (14)$$

Equation (9) may be solved numerically via an iterative method. The algorithm proceeds as follows. We begin with some reasonable initial approximation for $U_{\nu'}$. Using this, we compute $P'_{ic}(\gamma_e)$, $t'_c(\gamma_e)$ and $\gamma_{e,\min}$. Then, we compute the spectral distributions $P'_s(\nu', \gamma_e)$ and $P'_{ic}(\nu', \gamma_e)$ for all $\gamma_e \geq \gamma_{e,\min}$ and obtain via equation (9) a new approximation for $U_{\nu'}$. We take this $U_{\nu'}$, or (for smoother convergence) a suitable linear combination of the new and old $U_{\nu'}$, as the current approximation for $U_{\nu'}$ and repeat the steps. The iteration usually converges fairly quickly.

This approach can be combined with any desired model for the GRB fireball and afterglow dynamics. We have used the dynamics described in Sari et al. (1998), except that we multiplied the calculated fluxes by a factor of 1/4 (cf., Yost et al. 2003).

3.2 Dynamical approach

In this approach we follow dynamically the electron distribution as a function of time (Moderski et al. 2000). The main uncertainty is from the approximation for the initial distribution of the newly shocked electrons as a function of time. Lacking a better model, we assume that the electrons are accelerated at the shock wave initially to a single power law distribution:

$$Q = K\gamma_e^{-p} \text{ for } \gamma_m \leq \gamma_e \leq \gamma_M, \quad (15)$$

where the maximal Lorentz factor is given by $\gamma_M \approx 4 \times 10^7 B'^{-1/2}$ (Wei & Cheng 1997). The normalization factor satisfies: $K \approx 4\pi(p-1)R^2 n_m \gamma_m^{p-1}$, and n_m is the number density of the medium. We now follow the evolution of the electron distribution using:

$$\frac{\partial N_{\gamma_e}}{\partial R} + \frac{\partial}{\partial \gamma_e} (N_{\gamma_e} \frac{d\gamma_e}{dR}) = Q, \quad (16)$$

where

$$\frac{d\gamma_e}{dR} = -\frac{\sigma_T}{6\pi m_e c^2} \frac{B'^2}{\beta_\Gamma \Gamma} [1 + Y(\gamma_e)] \gamma_e^2 - \frac{\gamma_e}{R}, \quad (17)$$

Γ is the bulk Lorentz factor of the shocked medium, and $\beta_\Gamma = \sqrt{1 - 1/\Gamma^2}$, $B'^2/8\pi$ is the magnetic energy density. As usual, we assume that a fraction ϵ_e (ϵ_B) of the shock energy density is converted into energy of relativistic electrons (magnetic field).

To complete the calculations we need the location and the Lorentz factor of the blast wave as a function of time. The dynamics of the blast wave is obtained by solving the differential equations presented by Huang et al. (2000). The possible (but poorly understood) sideways expansion of the ejecta is ignored. We then calculate the electron distribution using eq. (16) and the supplemental relations. The quantity $n_{\nu'}$ needed in eq.(7) is calculated via (for simplicity, we consider only single scattering):

$$n_{\nu'} \approx \frac{T'}{h\nu'} \frac{\sqrt{3}\pi e^3 B'}{4m_e c^2} \int_{\gamma_{\min}}^{\gamma_M} n(\gamma_e) F\left(\frac{\nu'}{\nu'_s}\right) d\gamma_e, \quad (18)$$

where $n_{\gamma_e} \approx (4\Gamma + 3)N_{\gamma_e}/(4\pi R^3/3) \approx 3\Gamma N_{\gamma_e}/(\pi R^3)$ (The term $4\Gamma + 3$ is introduced by the shock jump condition), $T' \approx R/(12\Gamma c)$ is the time that the synchrotron radiation photons stay within the shocked medium, and $\gamma_{\min} \sim 3$ is the Lorentz factor below which the synchrotron approximation becomes invalid.

Once we know the energy distribution of the electrons, we calculate the synchrotron and inverse Compton emission, including synchrotron-self-absorption, and we integrate the observed flux over the “equal-arrival time surfaces” (Rees 1966; Waxman 1997; Sari 1998; Granot, Piran & Sari 1999). In the current code, we did not take into account the influence of the synchrotron-self-absorption on the electron distribution, as that done in Pe’er & Waxman (2005). However, with typical GRB afterglow parameters adopted in this work, for $10^2 \text{sec} < t < 10^3 \text{sec}$ (at late times, the high energy emission are usually too low to be of our interest), it is straightforward to show that the random Lorentz factor of the electrons emitting at the synchrotron-self-absorption frequency (Chevalier & Li 2000; Sari & Esin 2001) is < 100 . The modification of the low energy electron’s distribution through the synchrotron-self-absorption is thus unlikely to influence the high energy spectrum significantly.

In Fig. 2, we compare the spectral distributions calculated via the simple instantaneous approach of sec. 3.1 and the more detailed dynamical approach of this subsection. The two methods are clearly consistent with each other. This gives us confidence in the validity of both calculations. Note that the multiple inverse Compton scattering are ignored in our dynamical approach but are included in the instantaneous approximation. The consistence between these two approaches suggests that the multiple inverse Compton scattering is not important, at least for the typical GRB afterglow parameters (see also Sari & Esin 2001).

In the case of EIC, the seed photon energy distribution is not influenced by the electron energy distribution. From this point of view the calculations are simpler. However there is another complication, viz., for the cases of interest to us, the seed photons are highly anisotropic in the rest frame of the blast wave. The spectrum of radiation scattered at an angle θ_{sc} relative to the direction of the photon beam pene-

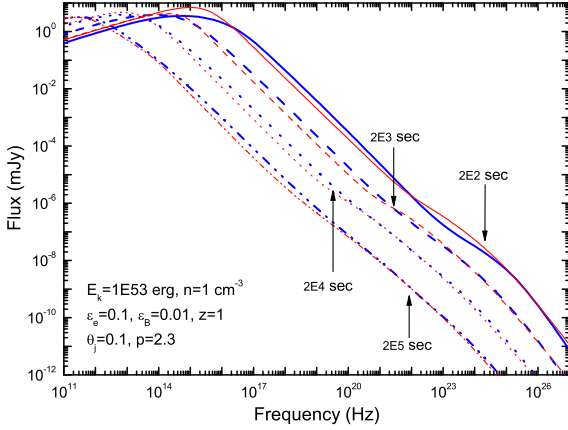


Figure 2. Comparison of afterglow spectra calculated with the instantaneous approximation (sec. 3.1, thin red lines) and the dynamical approach (sec. 3.2, thick blue lines). Model parameters are listed on the plot, and the timescales corresponding to each set of spectra are identified next to the curves. Note that all the results shown in later plots were obtained with the full dynamical approach.

trating through this region is (Aharonian & Atoyan 1981):

$$\frac{dN_\gamma}{dt dv'_{\text{EIC}} d\Omega'} \approx \frac{3\sigma_T c}{16\pi\gamma_e^2} \frac{n_\nu dv'}{\nu'} \left[1 + \frac{\xi^2}{2(1-\xi)} - \frac{2\xi}{b_\theta(1-\xi)} + \frac{2\xi^2}{b_\theta^2(1-\xi)^2} \right], \quad (19)$$

where $d\Omega' = 2\pi \sin\theta_{\text{sc}} d\theta_{\text{sc}}$, $\xi \equiv h\nu'_{\text{EIC}}/(\gamma_e m_e c^2)$, $b_\theta = 2(1 - \cos\theta_{\text{sc}})\gamma_e h\nu'/(m_e c^2)$, $\cos\theta_{\text{sc}} = (\cos\theta - \beta)/(1 - \beta\cos\theta)$, θ is the angle between the line of sight and the emitting point, β is the velocity of the emitting point, and $h\nu' \ll h\nu'_{\text{EIC}} \leq \gamma_e m_e c^2 b_\theta/(1 + b_\theta)$. As expected, on integration over θ_{sc} , eq. (19) reduces to eq. (7). The energy loss rate of the hot electron beam can be estimated by eq. (5) and $Y(\gamma_e)$ is governed by eqs. (1-7) for a given n_ν (see §5.2 for details).

4 HIGH ENERGY SSC AFTERGLOW

The dominant source of long lasting high energy GRB afterglow emission is SSC of the hot electrons in the forward external shock. At early stages when the cooling of most electrons is important, the luminosity of the SSC emission, L_{SSC} , is related to the luminosity of the synchrotron radiation, L_{syn} , as (Sari & Esin 2001):

$$L_{\text{SSC}} \sim \mathcal{Y} L_{\text{syn}}, \quad (20)$$

where \mathcal{Y} is the Compton parameter. The X-ray luminosity L_X is a small fraction of L_{syn} but we can use it as a proxy for the total luminosity. To do so we define a factor ϵ_X such that $L_X \equiv \epsilon_X L_{\text{syn}}$ and:

$$L_{\text{SSC}} \sim \mathcal{Y} L_X / \epsilon_X. \quad (21)$$

As long as ϵ_X does not vary significantly with time, we expect the broad-band SSC afterglow light curve and the X-ray

light curve to have a similar temporal behavior. We expect, therefore, that L_X and L_{SSC} should be highly correlated. This is, of course, confirmed by more detailed analysis, as shown below in eq. (32).

The light curve depends on the dynamics of the blast wave and in particular on the evolution with time of L_{eln} , the power given to the shocked electrons (see eq. 23). We consider first the evolution expected in the standard afterglow model and then discuss various modifications to the model.

4.1 Analytic Considerations

We begin with the standard afterglow. We consider a circum-burst medium with a number density profile $n_m = n_* R^{-k}$, $0 \leq k < 3$; here, $k = 0$ corresponds to a constant density ISM, and $k = 2$ to a standard stellar wind (Mészáros, Rees & Wijers 1998; Dai & Lu 1998b; Chevalier & Li 2000), though $k \sim 1.5$ is still possible, as found in some supernovae (Weiler et al. 2002) and in GRB 991208 (Dai & Gou 2001). The quantity n_* is the number density at a distance $R = 1$:

$$n_* = \begin{cases} n, & \text{for } k=0, \\ 3.0 \times 10^{35} A_* \text{ cm}^{-3}, & \text{for } k=2, \end{cases} \quad (22)$$

where $A_* = [\dot{M}/10^{-5} M_\odot \text{ yr}^{-1}][v_w/(10^8 \text{ cm s}^{-1})]$, \dot{M} is the mass loss rate of the progenitor, v_w is the velocity of the stellar wind (Chevalier & Li 2000).

Following the standard afterglow model, we assume that the dynamical evolution of the ejecta has a Blandford-McKee self-similar profile (Blandford & McKee 1976). The power given to the freshly shocked electrons, L_{eln} , in the blast wave is:

$$L_{\text{eln}} \approx \epsilon_{e,-1} E_{k,53} t_3^{-1} \begin{cases} 7.5 \times 10^{48} \text{ erg s}^{-1}, & \text{for } k=0; \\ 5 \times 10^{48} \text{ erg s}^{-1}, & \text{for } k=2. \end{cases} \quad (23)$$

where E_k is the equivalent isotropic energy of the ejecta. We note that L_{eln} depends only weakly on the density profile. Here and throughout this text, the convention $Q_x = Q/10^x$ has been adopted in cgs units.

The SSC luminosity can be estimated as:

$$L_{\text{SSC}} \approx \epsilon_{\text{high}} L_{\text{eln}}. \quad (24)$$

All the physics in this equation is, of course, hidden in the factor ϵ_{high} , which depends, in turn, on the synchrotron and cooling frequencies, ν_m and ν_c (Sari et al. 1998), and on the power law index of the electron distribution, p :

$$\epsilon_{\text{high}} \sim \eta \mathcal{Y} / (1 + \mathcal{Y}), \quad (25)$$

where (Sari et al. 1996; Sari & Esin 2001):

$$\eta \equiv \min\{1, (\nu_m/\nu_c)^{(p-2)/2}\}, \quad (26)$$

$$\mathcal{Y} \sim (-1 + \sqrt{1 + 4\bar{\eta}\epsilon_e/\epsilon_B})/2, \quad (27)$$

$$\bar{\eta} \equiv \min\{1, (\nu_m/\bar{\nu}_c)^{(p-2)/2}\}, \quad (28)$$

$$\bar{\nu}_c = (1 + \mathcal{Y})^2 \nu_c. \quad (29)$$

The ratio of the synchrotron and cooling frequencies satisfies (Sari et al. 1998; Yost et al. 2003):

$$\frac{\nu_m}{\bar{\nu}_c} \approx \begin{cases} 0.0024 C_p^2 \epsilon_{e,-1}^2 \epsilon_{B,-2}^2 n E_{k,52} t_3^{-1}, & \text{for } k=0, \\ 0.12 C_p^2 \epsilon_{e,-1}^2 \epsilon_{B,-2}^2 A_{*,-1}^2 t_3^{-2}, & \text{for } k=2, \end{cases} \quad (30)$$

where $C_p \equiv 13(p-2)/[3(p-1)]$. Note that, in all analytical relations, the time and the frequency are measured in the burst's frame, that is we ignore cosmological $(1+z)$ corrections. Numerical results are presented for a canonical burst at $z = 1$.

The X-ray band is typically above $\max\{\nu_m, \nu_c\}$. In this case the forward shock X-ray emission can be related to the kinetic energy of the forward shock (Kumar 2000; Freedman & Waxman 2001; Fan & Piran 2006a):

$$L_X \approx \epsilon_{B,-2}^{(p-2)/4} \epsilon_{e,-1}^{p-1} (1 + \mathcal{Y})^{-1} E_{k,53}^{(p+2)/4} t_3^{(2-3p)/4} \begin{cases} 8.8 \times 10^{47} \text{ ergs s}^{-1}, & \text{for } k = 0; \\ 1.4 \times 10^{48} \text{ ergs s}^{-1}, & \text{for } k = 2. \end{cases} \quad (31)$$

We thus have

$$\frac{L_{\text{SSC}}}{L_X} \sim 4\eta \mathcal{Y} \epsilon_{e,-1}^{2-p} \epsilon_{B,-2}^{(2-p)/4} E_{k,53}^{(2-p)/4} t_3^{3(p-2)/4} \begin{cases} 2, & \text{for } k = 0; \\ 1, & \text{for } k = 2, \end{cases} \quad (32)$$

For a universal $p \sim 2.1 - 2.3$, L_{SSC}/L_X is sensitive only to η and \mathcal{Y} and it is only weakly dependent on other parameters. At early times, when the cooling of electrons is important, $L_{\text{SSC}} \propto t_3^{3(p-2)/4} L_X$ (note that in the standard afterglow model, $E_k, n_*, \epsilon_e, \epsilon_B$ are all constant). Therefore a wide band SSC light curve will have a temporal behavior quite similar to that of the X-rays.

Roughly speaking, the energy of the SSC emission peaks at a frequency $\sim \max\{\nu_m^{\text{SSC}}, \nu_c^{\text{SSC}}\}$, where $\nu_m^{\text{SSC}} \approx 2\gamma_m^2 \nu_m$ and $\nu_c^{\text{SSC}} \approx 2\gamma_c^2 \nu_c$, where γ_c is the cooling Lorentz factor of shocked electrons. Following the standard treatment (Sari et al. 1998; Chevalier & Li 2000), we have

$$\nu_m^{\text{SSC}} \approx 10^{21} \text{ Hz } C_p^4 \epsilon_{e,-1}^4 \epsilon_{B,-2}^{1/2} \begin{cases} 6.2 n^{-1/4} E_{k,53}^{3/4} t_3^{-9/4}, & \text{for } k = 0; \\ 1.4 A_{*,-1}^{-1/2} E_{k,53} t_3^{-2}, & \text{for } k = 2, \end{cases} \quad (33)$$

$$\nu_c^{\text{SSC}} \approx 10^{24} \text{ Hz } (1 + \mathcal{Y})^{-4} \epsilon_{B,-2}^{-7/2} \begin{cases} 4 n^{-9/4} E_{k,53}^{-5/4} t_3^{-1/4}, & \text{for } k = 0; \\ 1.5 A_{*,-1}^{-9/2} E_{k,53}^2 t_3^2, & \text{for } k = 2. \end{cases} \quad (34)$$

Note that $\nu_c^{\text{SSC}} \propto n^{-9/4}$ or $\propto A_*^{-9/2}$. So $n \sim 10^3 \text{ cm}^{-3}$ or $A_* \sim \text{a few}$ will shift ν_c^{SSC} to the X-ray/UV/optical band and in this case the SSC emission will influence the X-ray observations. It may even cause a flattening of the X-ray light curve due to the emergence of this new component. An example of such a case is shown in Fig.3. One can see a flat X-ray segment, which is rather similar to that detected by *Swift*. However, it is not clear that this can account for the *Swift* observations because in this case the X-Ray spectrum would vary with time (see the insert of Fig.3). Such variations are not seen in the *Swift* data.

The (adiabatic) standard afterglow model assumes that (i) the outflow energy is a constant and (ii) the shock parameters are constant. As mentioned earlier this model is inconsistent with the shallow decline phase (phase-II). One possibility is that one of these two basic assumptions should be revised (Zhang et al. 2006; Fan & Piran 2006a; Ioka et al. 2006; Panaitescu et al. 2006; Nousek et al. 2006; Granot et al. 2006). We consider energy injection of the form $E_k \propto t^{1-q}$ (Cohen & Piran 1999; Zhang & Mészáros 2001a),

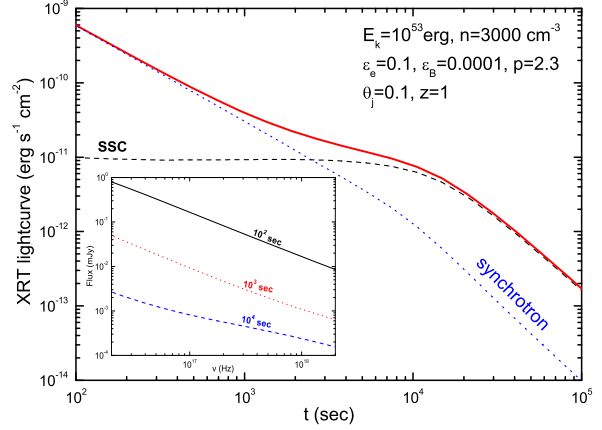


Figure 3. The XRT light curve in a dense ISM. The thick solid line is the predicted X-ray light curve, including both the synchrotron and the SSC components of the forward shock. The insert shows the corresponding X-ray spectra at three different times, as marked in the plot.

where $q = 1$ represents no energy injection and $q = 0$ corresponds to a pulsar/magnetar-like energy injection (Dai & Lu 1998; Zhang & Mészáros 2001a; Dai 2004; Fan & Xu 2006). Other q values are possible for an energy injection that results from slower material progressively catching up (Rees & Mészáros 1998; Kumar & Piran 2000; Sari & Mészáros 2000; Granot & Kumar 2006) or if an energy injection is caused by the fall-back of the envelope of the massive star (MacFadyen, Woosley & Heger 2001; Zhang, Woosley & Heger 2007). We also explore the situation where the equipartition parameters, ϵ_e and ϵ_B , are shock-strength dependent (i.e., time dependent)², though the underlying physics is far from clear (Piran & Fan 2007). Instead of exploring the possible physical processes that lead to such a phenomenon, we simply take $(\epsilon_e, \epsilon_B) \propto (t^c, t^d)$. These modifications lead to:

$$L_X \propto \frac{\eta \epsilon_X}{1 + \mathcal{Y}} t^{(c-q)}. \quad (35)$$

It is straightforward to show that

$$L_{\text{SSC}} \propto \frac{\eta \mathcal{Y}}{1 + \mathcal{Y}} t^{(c-q)}, \quad (36)$$

$$\nu_m^{\text{SSC}} \propto t^{4c + \frac{d}{2} + \frac{(6-k)(1-q) + (5k-18)}{2(4-k)}}, \quad (37)$$

$$\nu_c^{\text{SSC}} \propto t^{-\frac{7}{2}d + \frac{6(k-1)}{4-k} - \frac{(7k-10)}{2(4-k)}q} (1 + \mathcal{Y})^{-4}. \quad (38)$$

Equation (36) is one of our main results. As expected, with significant energy injection, or either ϵ_e increasing with time, or both, L_{SSC} (general) is flattened. An ϵ_B decreasing (increasing) with time will also flatten (steepen) the high energy emission light curve. However, such a modification seems to be small and it cannot give rise to either the observed shallow decline phase of the x-ray light curve or to a

² One may speculate that the energy distribution index of the accelerated electrons p is also time-evolving. However, this is not seen in the data as the spectrum does not vary during this phase.

detectable signature in the high energy component. Therefore, we focus on models with either time-dependent E_k or ϵ_e .

The shallow decline seen in the X-ray light curve during phase-II (Fig. 1) requires $q \sim 0.5$ or $c \sim 0.4$. In general, for $L_X \propto t^{-\alpha}$ ($\alpha \leq 1$) we need (in the energy injection case) $q = [4(\alpha + 1) - 2p]/(p + 2)$ which yields $L_{\text{SSC}} \propto t^{-[4(\alpha+1)-2p]/(p+2)} \propto t^{-\alpha}$ for $p \sim 2$. The high energy decline is quite similar to the decline of the X-rays. For a varying ϵ_e (with no energy injection, i.e., $q = 1$), we need $c = (3p - 2 - 4\alpha)/[4(p - 1)]$, which in turn results in $L_{\text{SSC}} \propto t^{(p+2-12\alpha)/[8(p-1)]} \propto t^{(1-3\alpha)/2}$ for $p \sim 2$. The high energy decline is slightly slower than that of the X-rays in this case.

At least in principle, one could combine IR/optical/UV/X-ray and high energy observations to distinguish between the two modifications described above. For example, we have $\nu_m \propto \epsilon_e^2 E_k^{1/2}$ and $\nu_m^{\text{SSC}} \propto \epsilon_e^4 E_k^{(6-k)/[2(4-k)]}$. If the early X-ray flattening was caused by $\epsilon_e \propto t^c$, ν_m and ν_m^{SSC} will decline much more slowly than in the energy injection case $E_k \propto t^{1-q}$. The wide energy range of LAT onboard GLAST (20MeV-300GeV) might enable us to observe the variations of ν_m^{SSC} with time.

It is interesting to note in passing that these modifications provide a possible explanation for some long-term puzzles in GRB 940217. The long-lasting MeV to GeV afterglow emission of GRB 940217 (Hurley et al. 1994) showed two remarkable features: (a) the count rate of high energy photons was almost a constant (b) the typical energy of these photons was nearly unchanged. These two features can be reproduced with $c = q \sim 1/2$ and $d = k = 0$ (Wei & Fan 2007).

4.2 Numerical Results

We turn now to numerical computations of the high energy light curves. We consider, first, the standard afterglow model using typical parameters that seem to fit the average late afterglow: $E_k = 10^{53}$ erg, $p = 2.3$, $\epsilon_e = 0.1$, $\epsilon_B = 0.003$ and $\theta_j = 0.1$. We consider a typical burst at $z = 1$. Figures 4 and 5 depict the calculated light curves and spectra for two models of the external medium: a uniform density ISM and a stellar wind. In both figures, panel (a) shows the SSC emission afterglow light curve and panel (b) shows the spectrum.

We consider now an energy injection model where the energy injection has the form:

$$dE_{\text{inj}}/dt = 5 \times 10^{49} (t/100\text{s})^{-0.5} \text{ erg s}^{-1} \quad (39)$$

for $10^2 \text{ s} < t < 10^4 \text{ s}$, which corresponds to $q = 0.5$ and $E_k = 10^{52}$ erg. Apart from q and E_k all other parameters are similar to those used in the standard case above. The total integrated energy injected is equal to $9 \times 10^{52} \text{ erg} \gg E_k$. The resulting light curve is shown in Fig. 6. The SSC light curve is flattened when the energy injection is strong enough to suppress the deceleration of the outflow. The numerical light curve has $L_{\text{SSC}} \propto t^{-(0.6 \sim 0.7)}$ which is consistent with our analytic estimate $L_{\text{SSC}} \propto t^{-0.5}$ for $c = 0$ and $q = 0.5$ (see eq. (36)).

We turn now to a time-evolving shock parameter ϵ_e , and consider ϵ_e varying as $t^{0.4}$. As shown in eq. (36) and in Fig. 7, an increase with time of ϵ_e flattens the high energy

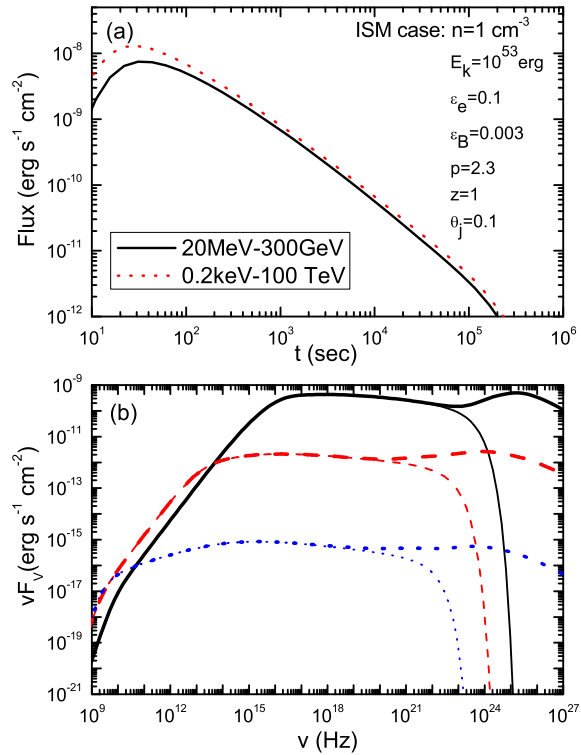


Figure 4. SSC radiation from the forward shock for the case of a constant density external ISM. (a) SSC light curves in the energy ranges 20MeV-300GeV and 0.2 keV-100 TeV, respectively. (b) Spectra at three selected times; thin and thick lines correspond to the pure synchrotron spectrum and SSC+synchrotron spectrum, respectively, and solid, dashed and dotted lines are at 2×10^2 , 2×10^4 and 2×10^6 s after the burst.

emission light curve. The very small ϵ_e at early time not only lowers the fraction of the shock energy given to the fresh electrons but it also suppresses the SSC emission. The resulting $t^{-0.5}$ decline depicted in Fig. 7 is consistent with the analytic estimate $t^{-0.4}$ for $c = 0.4$ (and $q = 1$).

To check the consistency of the numerical and analytic results, we plot the two estimates of L_{SSC} (using eq. 24) in Fig. 8. The analytic results (the thick lines) are a factor of 2–4 times larger than the corresponding numerical results (the thin lines). This is reasonable as some important corrections, such as the integration of the emission over “equal-arrival surfaces”, have been ignored in the analytic formulae.

5 HIGH ENERGY EMISSION ASSOCIATED WITH X-RAY FLARES

We turn now to GeV flares that might arise from inverse Compton scattering of the radiation associated with X-ray (or UV) flares. Although X-ray flares (phase-V in Fig.1) were detected even before *Swift*, their frequency became clear only after *Swift* began its observations. By now it is known that flares are quite common and can appear at all phases of the afterglow. At times the energy emitted in a flare can be fairly large. There are two main ideas to explain the origin of these flares: (i) “Late internal shocks” (Fan & Wei 2005,

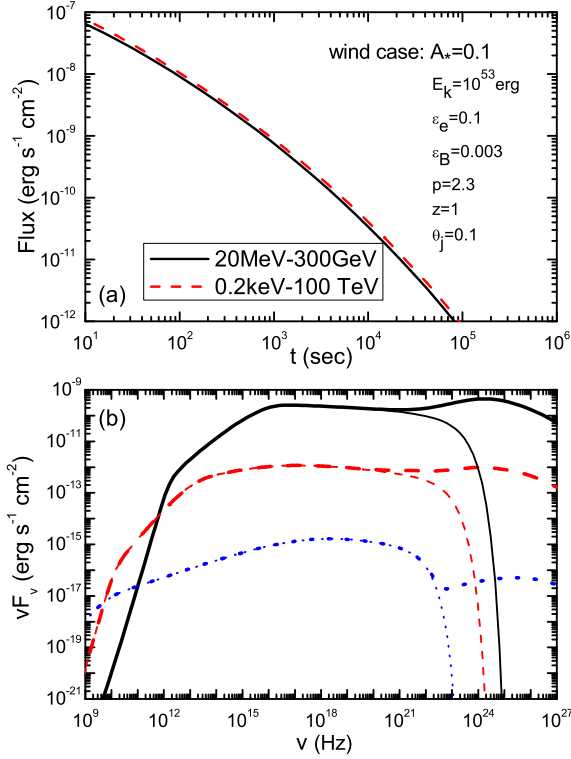


Figure 5. SSC radiation from the forward shock for the case when the external medium corresponds to the wind from the progenitor star ($k = 2$). The line styles are the same as in Fig. 4.

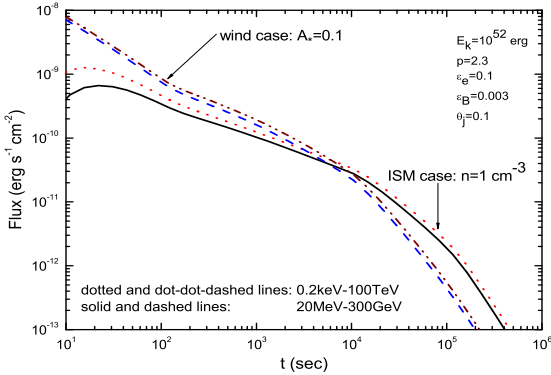


Figure 6. SSC radiation from the forward shock for the case when energy from the central engine is injected over a period of time: $dE_{\text{inj}}/dt = 5 \times 10^{49} (t/100\text{s})^{-0.5} \text{ erg s}^{-1}$ for $10^2 \text{ s} < t < 10^4 \text{ s}$. Note that the SSC emission light curve flattens as a result of the energy injection.

Burrow et al. 2005, Zhang et al. 2006) associated with a long-lived central engine, and (ii) "refreshed shocks" (Guetta et al. 2007) when late shells encounter the external shock and lead to brightening.

Inverse Compton scattering of photons from an X-ray flare are possible via two distinct mechanisms. It could be the result of SSC emission from the same electrons that pro-

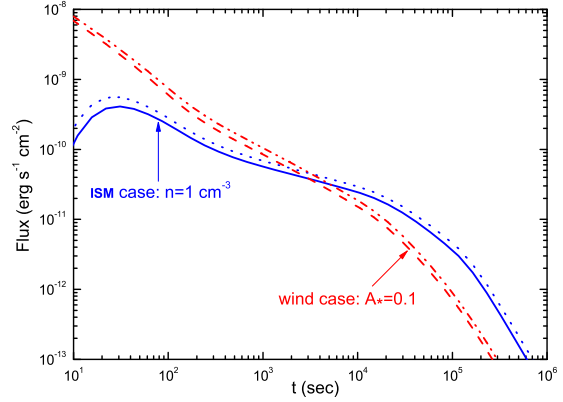


Figure 7. SSC radiation from the forward shock for the case when the electron energy parameter ϵ_e varies with time. The solid and dashed lines correspond to the emission in the energy range 20MeV-300GeV, while the dotted and dot-dot-dashed lines are for the emission in the energy range 0.2 keV-100 TeV. The shock parameters are $\epsilon_B = 0.003$, $\epsilon_e = 0.017$ for $t < 100 \text{ s}$, $\epsilon_e = 0.017(t/10)^{0.4}$ for $t < 10^4 \text{ s}$ after which it saturates. Other parameters are $E_k = 10^{53} \text{ erg}$, $z = 1$, $\theta_j = 0.1$, $p = 2.3$. The parameters corresponding to the external medium are marked on the plot.

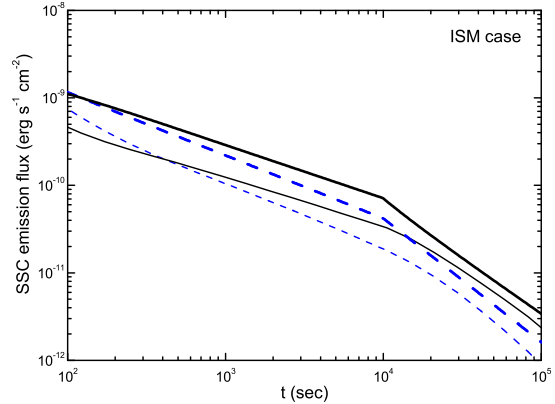


Figure 8. Comparison of numerical and analytical results for ISM. The thin lines are our numerical SSC light curves for the energy range 0.2keV – 100TeV, while the thick lines are the corresponding analytical results. The solid and dashed lines are the results in the cases of energy injection and ϵ_e increasing with time, respectively. The parameters are the same as in Fig. 6 and in Fig. 7, respectively. For the wind medium, the results are rather similar.

duce the X-ray flares. If the X-ray flare is produced by late internal shocks, then an additional source of high energy radiation is possible, viz., EIC scattering of flare photons by hot electrons in the external shock. We consider both possibilities.

5.1 SSC flares

SSC within the same shock that produces the X-ray flare will give a high energy flare simultaneously with the low

energy flare. This would arise if the X-ray flare results from either a late internal shock or from a refreshed shock within the forward external shock.

It is difficult to predict the expected SSC emission as we have no robust estimate of the typical Lorentz factor of the shocked electrons that produce the X-ray flare. A critical factor is the location of the shock, which determines the various parameter within the emitting region. For prompt γ -rays from an internal shock, the typical radius of the shock is $R_{\text{prompt}} \sim 10^{13} - 10^{15}$ cm (Piran 1999; Piran 2004). If flares are produced by “late internal shocks”, $R_{\text{flare}} \sim 10^{15}$ cm is possible (Fan & Wei 2005), whereas with “refreshed external shocks”, R_{flare} may be as large as 10^{17} cm (Galli & Piro 2007; Wu et al. 2007; Guetta et al. 2007).

Assuming that the soft X-ray flares are powered by the synchrotron radiation of the shocked electrons we can estimate the typical Lorentz factor of the electrons, $\gamma_{e,m}$. The magnetic field, B , at R_{flare} can be estimated by:

$$\begin{aligned} B &\sim [2\varepsilon L_X / (\Gamma^2 R_{\text{flare}}^2 c)]^{1/2} \\ &\sim 250 \text{ Gauss } \varepsilon^{1/2} L_{X,49}^{1/2} \Gamma^{-1} R_{\text{flare},17}^{-1}, \end{aligned} \quad (40)$$

where $\varepsilon \equiv \epsilon_B / \epsilon_e$. For this value of the magnetic field, the peak energy of the flare photons will be at $E_p \sim 0.2$ keV if the typical electron Lorentz factor is

$$\gamma_{e,m} \sim 800 \varepsilon^{-1/4} L_{X,49}^{-1/4} R_{\text{flare},15}^{1/2} (E_p / 0.2 \text{ keV})^{1/2}. \quad (41)$$

The energy of a typical inverse Compton photon is then

$$\begin{aligned} h\nu_p^{\text{SSC}} &\sim 2\gamma_{e,m}^2 h\nu_p \\ &\sim 0.3 \text{ GeV } \varepsilon^{-1/2} L_{X,49}^{-1/2} R_{\text{flare},15} (E_p / 0.2 \text{ keV})^2. \end{aligned} \quad (42)$$

Thus, high energy emission simultaneous with the X-ray flare is expected if the emitting region is not significantly magnetized.

Roughly speaking, the total fluence of the SSC emission of the flare shock is comparable to that of the X-ray emission, typically $10^{-7} \sim 10^{-6}$ erg cm $^{-2}$ integrated over the afterglow. In late internal shocks (i.e., $R_{\text{flare}} \sim 10^{15}$ cm), a GeV flash accompanying the X-ray flare is possible (Wei, Yan & Fan 2006). This problem was also discussed by Wang et al. (2006), who assumed that $\gamma_{e,m} \sim 100$ and obtained $h\nu_p^{\text{SSC}} \sim 10$ MeV, which they considered as uninteresting. However, as shown above, $\gamma_{e,m}$ can be large to ~ 1000 and $h\nu_p^{\text{SSC}}$ is two orders of magnitude larger. In refreshed external shocks, a GeV-TeV flash is predicted because of its very large R_{flare} ($\sim 10^{17}$ cm), as indicated in eq. (42). More detailed analysis can be found in Galli & Piro (2007).

A subtle issue that has to be checked is whether the high energy photons will be absorbed by pair production on the high energy tail of the flare. The pair production optical depth for photons with energy E_{cut} (absorbed by the flare photons with energy $E_a \sim 2(\Gamma m_e c^2)^2 / E_{\text{cut}} \sim 0.5 \text{ MeV } \Gamma_{1.5}^2 (E_{\text{cut}} / 1 \text{ GeV})^{-1}$) can be estimated as (e.g., Svensson 1987)

$$\begin{aligned} \tau_{\gamma\gamma} &\simeq \frac{11\sigma_T N_{>E_a}}{720\pi R_{\text{flare}}^2} \\ &\sim 4 \times 10^{-2} R_{\text{flare},15}^{-2} F_{\text{flare},-8.3} \delta t_1 D_{L,28.34}^2 \\ &\quad \left(\frac{E_p}{0.2 \text{ keV}} \right)^{\beta_{\text{flare}}-1} \Gamma_{1.5}^{-2\beta_{\text{flare}}} \left(\frac{E_{\text{cut}}}{1 \text{ GeV}} \right)^{\beta_{\text{flare}}}, \end{aligned} \quad (43)$$

where $N_{>E_a} = \frac{\beta_{\text{flare}}-1}{\beta_{\text{flare}}} \left(\frac{E_p}{E_a} \right)^{\beta_{\text{flare}}} \frac{4\pi D_L^2 F_{\text{flare}} \delta t}{E_p}$ is the total

flare photon number of one pulse satisfying $h\nu > E_a$, where δt is the timescale of the flare pulse and the high-energy power-law index $\beta_{\text{flare}} \sim 1.2$ has been used to get the numerical coefficient. Clearly, for $R_{\text{flare}} \sim 10^{17}$ cm, i.e., the refreshed shock case, the tens GeV high energy photon emission will not be absorbed by the flare photons. For $R_{\text{flare}} \sim 10^{15}$ cm, i.e., the late internal shock case, the small optical depth will not affect the sub-GeV flux unless $\delta t_1 > 25 \Gamma_{1.5}^{2\beta_{\text{flare}}} R_{\text{flare},15}^2$.

5.2 Extended EIC plateau

We turn now to the scenario in which the X-ray flares are produced by late internal shocks (Fan & Wei, 2005; Burrow et al. 2005; Zhang et al. 2006). We calculate the inverse Compton scattering of these seed photons by hot electrons accelerated within the external shock. We assume that the X-ray flares are accompanied by far-UV emission and calculate the upscattering of these photons as well. A central ingredient of this scenario is that in the rest frame of the blast wave, the seed photons are highly beamed. We take care of this effect, following the analysis of Aharonian & Atoyan (1981).

If the EIC emission is simultaneous with the X-ray flare (i.e., the duration of the EIC emission has not been extended significantly), the EIC luminosity can be estimated by eq. (24). However, in the rest frame of the shocked material, the EIC emission has a maximum at $\theta_{\text{sc}} = \pi$ and it vanishes for small scattering angles (Aharonian & Atoyan 1981; Brunetti 2001). This effect lowers the high energy flux in two ways. First, a fraction of the total energy is emitted out of our line of sight and thus the received power is depressed (relative to the isotropic seed photon case). This yields a correction by a factor of 2 (which we ignore henceforth). Second and more important, the strongest emission is from³ $\theta \sim 1/\Gamma$. Thus the peak time of the high energy EIC emission is estimated to be (Fan & Piran 2006b; Wang & Mészáros 2006):

$$T_p \sim R / (2\Gamma^2 c) \sim (4 - k)t_f, \quad (44)$$

where t_f is the time when the X-ray flare ceases. T_p , which is also proportional to the duration of the high energy peak, could be much longer than ΔT , the duration of the soft X-ray flare.

The luminosity of the high energy flare would be lower than the simple estimate by the ratio of the durations:

$$L_{\text{EIC}} \sim \frac{L_{\text{eln}}}{(T_p / \Delta T)}. \quad (45)$$

At 100-1000 s after the burst, the forward shock emission peaks in the far-UV to soft X-ray band, and the corresponding SSC emission peaks in sub-GeV to GeV energy range. A comparison of the SSC luminosity of the forward shock after but around t_f , L_{SSC} (eq. (24)), with L_{EIC} shows that

³ This could be more easily understood in the Thomson regime. As shown in eq.(43) of Brunetti (2001), in the local frame of the shocked medium, the emissivity is proportional to $(1 - \cos \theta_{\text{sc}})^{(1+\delta)/2}$, where $\delta = p$ or $p + 1$, depending on the cooling of the electrons. The observed emission from an angle θ is thus $\propto [\Gamma(1 - \beta \cos \theta)]^{-3} \sin \theta (1 - \cos \theta_{\text{sc}})^{(1+\delta)/2} \propto \theta^{\delta+2} (1 + \Gamma^2 \theta^2)^{-(7+\delta)/2} \equiv \mathcal{F}$ since $\cos \theta_{\text{sc}} = (\cos \theta - \beta) / (1 - \beta \cos \theta)$. The requirement that $d\mathcal{F}/d\theta = 0$ yields $\theta \approx \sqrt{(2+\delta)/5} / \Gamma \sim 1/\Gamma$ for $\delta \sim 2 - 3$.

the SSC emission would be stronger than the EIC emission and the wide EIC flare would be undetectable.

However, if the forward shock electrons are in the slow cooling regime before the X-ray flare, their SSC emission is weak and the EIC flare might be detectable. In this case the total energy available for extraction in the EIC process $\sim L_{\text{eln}}\Delta T + N_e\Gamma \min\{\gamma_c, \gamma_m\}m_e c^2$ is much larger than $\sim L_{\text{eln}}\Delta T$, where N_e is the total number of electrons swept by the forward shock at the time $\sim t_f - \Delta T$ and at the same time L_{SSC} is much smaller than L_{eln} . Though L_{SSC} may still outshine L_{EIC} at $t \sim t_f$, since it decreases rapidly with time (steeper than t^{-1} , as both η and $\mathcal{Y}/(1 + \mathcal{Y})$ are decreasing with time, see eq. (24)), the EIC high energy emission may still dominate at late times.

If the EIC emission dominates over the SSC emission, the high energy light curve will flatten, as we show below (e.g., Fig. 11). Such a flattening could arise also as a result of energy injection or due to an increasing ϵ_e . However, as we argued in the last section, in those two scenarios, the X-ray and the high energy emission light curves are quite similar and flattening should be apparent also in the X-ray signal. The EIC emission should, on the other hand, show an X-ray flare preceding high energy emission and not accompanying a flat X-ray light curve.

As an example we consider the giant flare of GRB 050502b (Burrows et al. 2005; Falcone et al. 2006) and examine the expected external IC emission that will arise from such a flare. The flux of the flare, in the 0.2–10 keV energy band, can be approximated as a steep rise: $F_{\text{flare}} \approx 5 \times 10^{-9} \text{ erg s}^{-1} \text{ cm}^{-2} (t/680\text{s})^7$ for $300\text{s} < t < 680\text{s}$, a constant plateau lasting until $\sim 800\text{s}$ and a subsequent sharp decline which might be due to a curvature emission component (Liang et al. 2006). To calculate the EIC emission we need (see eq. 7) $n'_{\nu'}$, the distribution of the seed photons in the rest frame of the shocked medium.

If the flare originates from activity of the central engine (Fan & Wei 2005; Zhang et al. 2006) one might expect that the radiation process is similar to that of the prompt emission. Lacking exact information on the spectrum of the flare and in particular on its peak energy we assume that it has a typical Band function (Band et al. 1993):

$$n_{\nu'} = A \begin{cases} \left(\frac{h\nu'}{1 \text{ keV}}\right)^{-(1+\alpha_{\text{flare}})} \exp(-\nu'/\nu'_p), \\ \left(\frac{Bh\nu'_p}{1 \text{ keV}}\right)^{\beta_{\text{flare}} - \alpha_{\text{flare}}} \exp(-\beta_{\text{flare}} - \alpha_{\text{flare}}) \left(\frac{h\nu'}{1 \text{ keV}}\right)^{-(1+\beta_{\text{flare}})} \end{cases}$$

where the high-energy power-law index $\beta_{\text{flare}} \approx \text{const} \sim 1.2$ and the low-energy power-law index $\alpha_{\text{flare}} \approx \text{constant} \sim 0$. As the peak energy is not known we consider three representative values: $E_p = 0.02, 0.2, 2\text{keV}$.

For a given ν'_p , the parameter A in eq. (46) is obtained from the observed flux:

$$\int_{0.02\text{keV}/h\Gamma}^{100\text{keV}/h\Gamma} n_{\nu'} h\nu' d\nu' \approx \frac{D_L^2 F_{\text{flare}}}{2R^2 \Gamma^2 c}, \quad (47)$$

where we used lower and upper limits on $h\nu'$ of $20\text{eV}/\Gamma$ and $100\text{keV}/\Gamma$. This is because the self-absorption frequency is likely to be in the UV band (Fan & Wei 2005) and the emission in the hard X-ray band is unknown for nearly all flares.

The redshift of GRB 050502b is unknown. We assume the canonical value of $z = 1$ for which $E_k \sim 10^{52} \text{ erg}$ because the γ -ray fluence is $\sim 10^{-6} \text{ erg cm}^{-2}$ (Burrows et

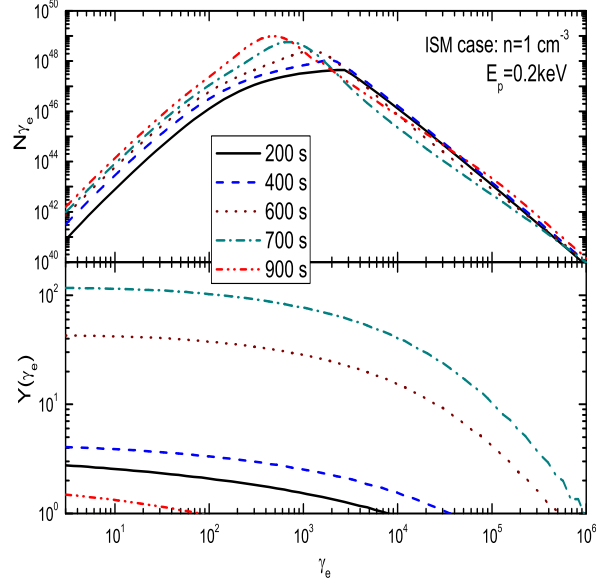


Figure 9. The electron distribution N_{γ_e} and the Compton parameter $Y(\gamma_e)$ as functions of the electron Lorentz factor γ_e . The flare photons are assumed to scatter off electrons in the forward shock for the case of a uniform external ISM. Different lines represent different times after the initial burst, as indicated in the figure; the times are determined by $dt = (1 + z)dR/(2\Gamma^2 c)$. The parameters of the model are: $E_k = 10^{52} \text{ erg}$, $n = 1 \text{ cm}^{-3}$, $z = 1$, $p = 2.3$, $\epsilon_e = 0.1$ and $\epsilon_B = 0.01$. The parameters of the flare are described in the text and the peak energy of the flare emission is taken to be $E_p \sim 0.2 \text{ keV}$.

al. 2005). For the other parameters we take $n = 1 \text{ cm}^{-3}$, $p = 2.3$, $\epsilon_e = 0.1$, $\epsilon_B = 0.01$, and $\theta_j = 0.1$. Figures 9 and 10 depict the electron distributions and the Compton parameters as functions of γ_e , for $E_p \sim 0.2 \text{ keV}$. The cooling effect of the X-ray flare photons on the blast wave electrons is seen clearly in these figures. One sees that the energy of the electrons is depressed between 400 and 700 s and then it increases at 900 s when the cooling effect due to the flare photons ceases. As expected the higher the flare luminosity, the stronger the EIC cooling. Electrons with $\gamma_e < 10^6$ lose most of their energy via the EIC process (see the large values of the Compton parameter for these electrons in Figs. 9(b) and 10(b)).

The resulting high energy emission is shown in Fig. 11. The SSC emission decreases during and after the flare as the electrons are cooled by the EIC process. Also at a later time we get contributions to the observed spectrum from higher latitude regions from which the emission is weaker. The EIC emission is not simultaneous with the X-ray flare. It peaks at $\sim (4 - k)t_f$ (see eq. (44)), and it lasts much longer than the X-ray flare. This temporal behavior is determined by the geometry of the emitting surface, the radiation spectrum and the highly anisotropic EIC emission. The lagging behavior is unique and if it is observed, i.e., if it is not hidden by SSC emission, it would demonstrate that X-ray flares are produced by internal shocks. Note that without the anisotropic correction, the EIC light curve is higher and narrower and

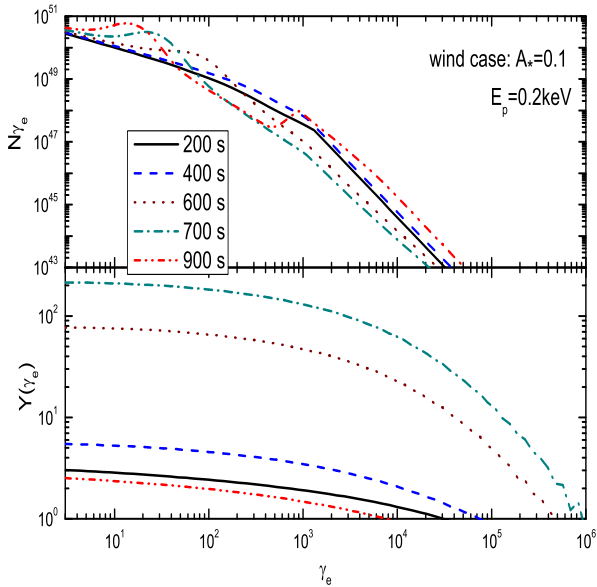


Figure 10. The electron distribution N_{γ_e} and the Compton parameter $Y(\gamma_e)$ as functions of the electron Lorentz factor γ_e . Here the flare photons are assumed to scatter off electrons in the forward shock for the case when the external medium is due to a stellar wind with $A_* = 0.1$. Other parameters are the same as in Fig. 9.

the peak EIC emission is overestimated by one order of magnitude (see Fig.12).

For most soft X-ray flares, the peak emission energy seems to be below 0.2 keV, i.e., they may be intrinsically far-UV flares. The up-scattering of the far-UV photons in the external blast wave results in strong sub-GeV emission. Fig. 13 depicts the resulting EIC spectrum (time integral) for different values of $E_p = (0.02, 0.2, 2)$ keV—other parameters, including the luminosity of the flare in the 0.2–10keV band are taken to be the same. For a far-UV flare ($E_p \leq 0.2$ keV) the seed photons are much more numerous than for an X-ray flare. Consequently the resulting sub-GeV photons are much more numerous than those resulting from a keV flare. Therefore the EIC emission following a UV flare will be easier to detect.

6 DETECTABILITY OF HIGH ENERGY EMISSION IN THE AFTERGLOW

We turn now to the key question: Are the GeV to TeV high energy signals predicted by our models observable with current or soon to be commissioned detectors?

Using the calculated high energy spectrum $F_\nu(t)$ as a function of time for any given model, we can estimate the total number, N_{det} , of detectable high energy photons,

$$N_{\text{det}} = \int_{t_I}^{t_E} \int_{\nu_d}^{\nu_u} \frac{F_\nu(t)}{h\nu} S_{\text{det}}(\nu) dt d\nu, \quad (48)$$

where $t_{I,E}$ are the times when the observations begin and

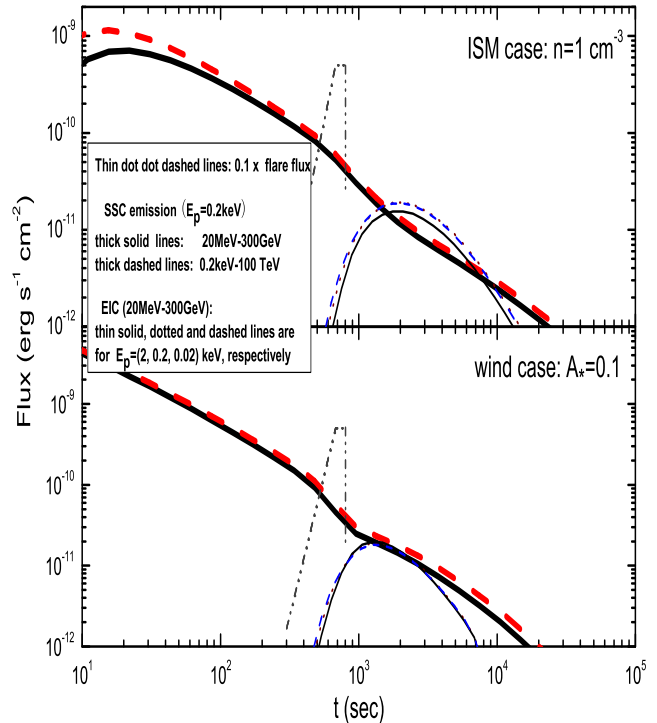


Figure 11. High energy light curve arising from flare photons scattering off the forward shock for the ISM/wind case (upper/lower panel), respectively. The parameters are the same as in Figs. 9 and 10, except for E_p which takes the values marked in the figure.

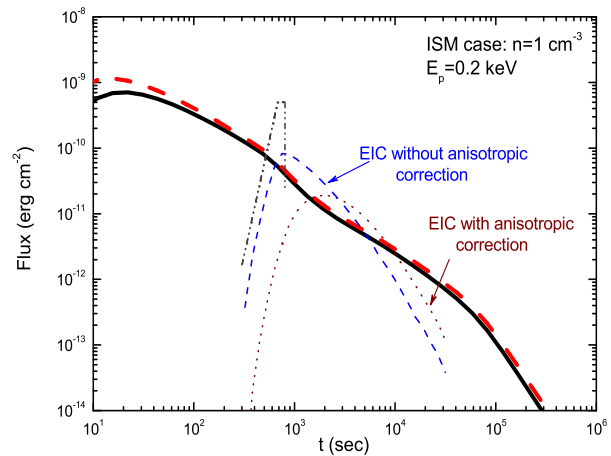


Figure 12. The EIC emission with (the dotted line) and without (the thin dashed line) anisotropic correction. Other lines and the parameters are the same as in the upper panel of Figs. 11, except for E_p that marked in the figure.

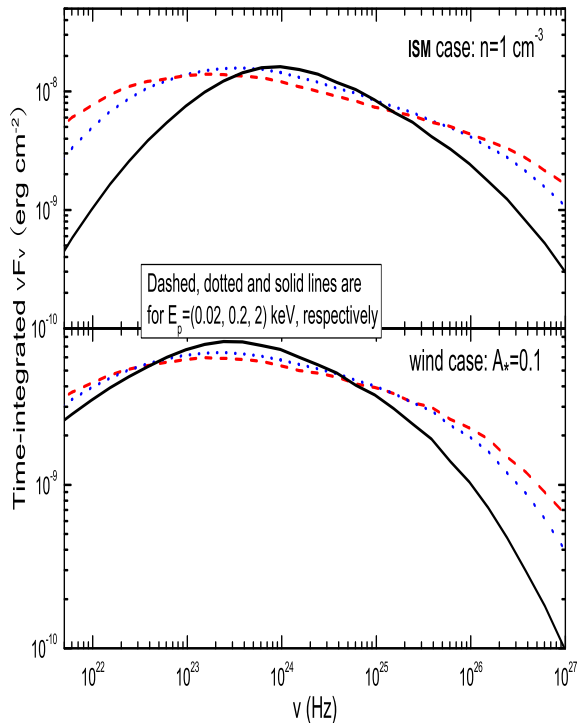


Figure 13. The EIC spectrum resulting from upscattering of flare photons by forward shock electrons. The parameters used are the same as in Fig. 9 and Fig. 10, except for E_p which takes the values marked in the figure.

end, respectively, $h\nu_d - h\nu_u$ is the energy range of the detector, and $S_{\text{det}}(\nu)$ is the effective area of the detector as a function of ν . For LAT onboard GLAST, we approximate $S_{\text{det}}(\nu)$ as (see http://www-glast.slac.stanford.edu/software/IS/glast_lat_performance.htm):

$$S_{\text{det}}(\nu) = \begin{cases} 500 \text{ cm}^2 (h\nu/20\text{MeV}), & \text{for } h\nu < 400\text{MeV}; \\ 10^4 \text{ cm}^2, & \text{for } h\nu \geq 400\text{MeV}. \end{cases} \quad (49)$$

We consider first the high energy SSC emission in the afterglow, which we estimated in sec. 4. For the models presented in Fig. 4 – Fig. 7, we use $t_1 \sim 100$ s; at earlier time the high energy emission may be dominated by the synchrotron and/or SSC emission of the internal shocks (Gupta & Zhang 2007). We choose an upper limit of $t_E \sim 4 \times 10^4$ s; after this time the SSC emission is usually too low to be of interest.

Figure 14 shows the integrated flux expected for the various SSC scenarios discussed in sec. 4, and Table 1 summarizes the expected number of photons that would be detected by LAT from a burst with standard parameters (see Figs. 4 - 7) at $z = 1$. Typically, one expects to detect a few photons above 20 MeV and very few high energy photons above 100 GeV.

Not surprisingly, the modified afterglow models that account for the shallow X-ray light curve in phase-II give fewer counts than the standard afterglow model. The reduced X-ray flux in these models (needed to explain the shallow light curve) causes a corresponding reduction in the high energy

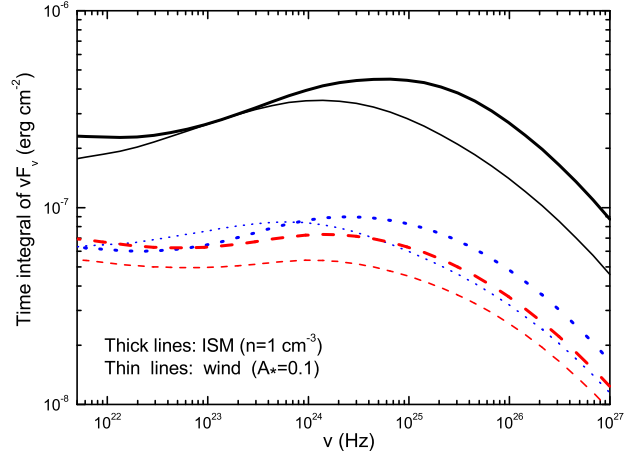


Figure 14. The integral of νF_ν in the time interval $100 - 4 \times 10^4$ s after the burst. The solid, dotted and dashed lines correspond to the standard afterglow model (Figs. 4 and 5), the energy injection model (Fig. 6) and the increasing ϵ_e model (Fig. 7), respectively.

flux. However, we still expect a weak detection by GLAST. Such weak signals, of course, cannot play an important role on distinguishing between the different models. But for some extremely bright events, e.g., GRB 940217, the high energy observation may pose a tight constraint on the underlying physical process (e.g., Wei & Fan 2007).

Considering next the high energy emission associated with flares, the time-integrated νF_ν of the high energy EIC component is shown in Fig. 13. In the case of a uniform external ISM, for $E_p = (0.02, 0.2, 2)$ keV, $N_{\text{det}}(> 20\text{MeV}) = (0.6, 0.5, 0.2)$ and $N_{\text{det}}(> 100\text{GeV}) = (3.2, 3.2, 2.6) \times 10^{-4}$, respectively. The EIC high energy afterglow component is more easily detected if the flare has a significant UV component. Note that Fan & Piran (2006b) used a larger effective detection area ($S_{\text{det}} \sim 8000\text{cm}^2$ in the energy range of 20MeV – 300GeV). This overestimates S_{det} for $h\nu < 100\text{MeV}$ where most of the up-scattered photons are expected (see eq. 49). In the case of an external shock in a stellar wind we have for $E_p = (0.02, 0.2, 2)$ keV, $N_{\text{det}}(> 20\text{MeV}) = (0.3, 0.3, 0.2)$ and $N_{\text{det}}(> 100\text{GeV}) = (1.7, 1.5, 1.0) \times 10^{-4}$, respectively. Now the scattered far-UV photons are in the sub-MeV band (Fan & Piran 2006b). Therefore, the far-UV component does not increase the detected signal.

As long as the flare outflow is just weakly or even not magnetized and $R_{\text{prompt}} \geq 10^{14}$ cm, the GeV SSC emission fluence is expected to be comparable to the fluence of the keV flare, typically $10^{-7} - 10^{-6}$ erg cm^{-2} . With such a fluence, the GeV flashes (SSC emission) accompanying bright flares may be detectable by GLAST. If the flare is produced by a late internal shock we expect that the typical SSC photon energy is about 300 MeV. At this energy a fluence $\sim 2.4 \times 10^{-3}/S_{\text{det}} \sim 3 \times 10^{-7}$ erg cm^{-2} corresponds to a detection of 5 photons. So the SSC emission of a very bright X-ray flare with a fluence $\sim 10^{-6}$ erg cm^{-2} should be detected, provided that the Compton parameter is unity or larger. If the flare is produced by a refreshed shock the typical photon energy would be higher, up to tens of GeV.

Table 1. Expected signal for GLAST from SSC emission of a GRB forward shock, where the absorption of the very high energy photons by IR background is ignored. These values we calculate for a typical burst with $E_k \sim 10^{53}$ erg (at the end of the X-ray shallow decline) and $z = 1$, correspondingly to the burst with a γ -ray fluence of $\sim 10^{-5}$ erg cm^{-2} .

	$N_{\text{det}}(> 20\text{MeV})$	$N_{\text{det}}(> 100\text{GeV})$
standard afterglow: ISM (Fig.4)	~ 13	~ 0.015
standard afterglow: wind (Fig.5)	~ 11	~ 0.008
energy injection: ISM (Fig.6)	~ 3.3	~ 0.003
energy injection: wind (Fig.6)	~ 3.6	~ 0.002
time increasing ϵ_e : ISM (Fig.7)	~ 3.3	~ 0.002
time increasing ϵ_e : wind (Fig.7)	~ 2.6	~ 0.001

The number of these high energy photons would then be much smaller than in the case of late internal shocks. As a result, it might not be detectable by GLAST.

So far we have focused on the detectability of high energy emission by GLAST. However, there are also other detectors. MAGIC⁴, Whipple⁵, H.E.S.S. ⁶ and Kangaroo⁷ are high energy telescopes operating at energies above 100 GeV. These Cerenkov detectors have very large effective areas $\sim 10^4 - 10^5 \text{m}^2$. The expected fluxes of very high energy ($> 100\text{GeV}$) photons from bursts at $z \approx 1$ should correspond to the detection of 10 – 100 photons. However, this estimate ignores the absorption of the high energy photons by the IR-background (Nikoshov 1962). Given that the optical depth for a 100 GeV photon from $z = 3$ is > 5 (Primack et al. 2005), we expect that for most *Swift* bursts with a typical $z \sim 2.8$ the number of detectable $> 100\text{GeV}$ photons will be negligible. Our results are thus largely consistent with the null detection of the MAGIC telescope (Albert et al. 2007). Whipple (Horan et al. 2007) observed the $> 400\text{GeV}$ afterglow emission of a few GRBs with $z \leq 1$, and in particular GRB 030329, a nearby long burst. However, the earliest observation was carried out ~ 64.55 hours after the trigger of GRB 030329 when the expected very high energy SSC afterglow emission is quite low (see also Xue et al. 2008). As the optical depth for IR absorption increases strongly with energy and at low redshifts linearly with z , we expect a detection of 100 GeV or lower energy photons from nearby strong bursts, provided the observations begin very early and last for several hours. Such nearby bursts are, of course, very rare but they do exist and high energy observatories should focus on them.

7 SUMMARY AND DISCUSSION

Very high energy inverse Compton emission is an integral part of the current afterglow model (Mészáros & Rees 1994; Dermer et al. 2000; Sari & Esin 2001; Zhang & Mészáros 2001b; Gou & Mészáros 2007; Galli & Piro 2007; Yu, Liu & Dai 2007; Beloborodov 2005; Fan et al. 2005b; Wang et al. 2006; Fan & Piran 2006b). We have calculated the high energy emission in different models of GRB afterglows, including the SSC component of the forward shock, the SSC

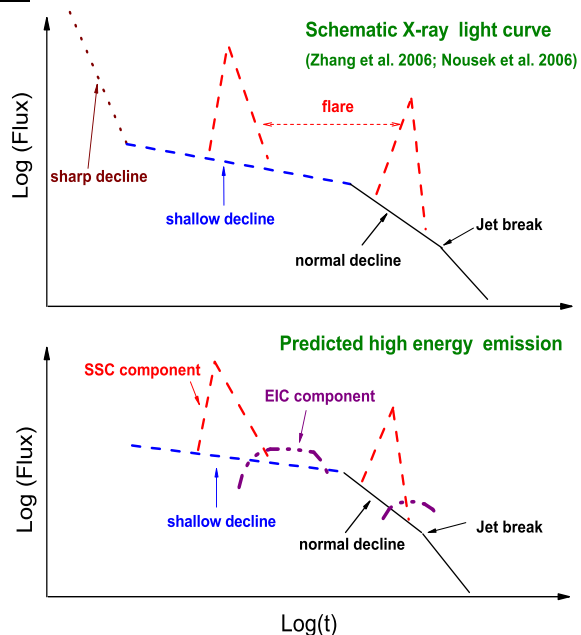


Figure 15. Summary of the results. The expected high energy afterglow signatures are shown in the lower panel, corresponding to the schematic X-ray afterglow light curve shown in the upper panel. Note that the EIC emission light curve could be outshined by the SSC emission of the forward shock. The SSC emission of the X-ray flares might be weak if the emission region is significantly magnetized or R_{flare} is much smaller than 10^{14} cm.

component of the electrons producing X-ray flares and the EIC component of flare photons upscattered by relativistic electrons in the forward shock. Our predicted high energy light curves are summarized schematically in the lower panel of Fig. 15.

High energy SSC emission in the energy range 20 MeV – 300 GeV from bright bursts should lead to a detectable signal of several (≈ 10) photons by the LAT onboard GLAST. Higher energy telescopes such as MAGIC, Whipple, H.E.S.S and Kangaroo working in the energy range $> 100\text{GeV}$, could detect strong signals (few hundred photons) from nearby bursts at around the lower energy limit of these detectors ($\sim 100\text{GeV}$). Signals from more distant bursts will be absorbed by the IR background. The flux from a $z > 1$ burst will usually be too low to be detected.

Strong GeV SSC emission simultaneous with keV flare

⁴ <http://wwwmagic.mppmu.mpg.de/>

⁵ http://veritas.sao.arizona.edu/old/VERITAS_whipple.html

⁶ <http://www.mpi-hd.mpg.de/hfm/HESS/HESS.html>

⁷ <http://www.gridbus.org/raj/hepgrid/>

photons is possible if the emitting region is not highly magnetized⁸. The EIC component of the flare, on the other hand, will be extended and will last up to ten times as long as the X-ray flare (see Fig. 11)⁹. This is because, in the EIC process, the duration of the high energy emission is affected by the spherical curvature of the blast wave and is mainly extended by the highly anisotropic radiation of the up-scattered photons (see Fig.12). Unfortunately, a significant detection is likely only if the SSC emission of the forward shock is very weak. A high energy detection could be used to probe the spectrum of the low energy flare and in particular the possible existence of a far UV component. These signatures of the high energy flare are independent of the density profile of the external medium.

A detection of a high energy component, *in principle*, will enable us to test current models of GRBs and their afterglows. A detailed comparison of the high energy and low energy light curves, in particular during the shallow decline phase, might even enable us to discriminate between different modifications of the standard afterglow model. However, given the small number of expected high energy photons, it is unlikely that we can achieve this goal with GLAST.

It should be noted that the two modifications to the standard model that we considered in this paper, viz., extended energy injection and time-evolving ϵ_e , both predict achromatic behavior such that there should be a shallow light curve in the optical band simultaneously with the shallow X-ray light curve. However, as noted in Fig. 1, this is not always seen. Thus, it is possible that none of our models gives a correct description of afterglow physics. Model that suggest flattening of the light curve due to emergence of an X-ray SSC component (see Fig. 3) that would arise in a very dense medium may explain the X-ray flattening but this would involve significant variability in the observed X-ray spectrum.

One intriguing possibility is that the standard afterglow model, without energy injection or varying ϵ_e , is indeed the correct model, but the X-ray emission is suppressed during phase-II because of some radiation physics that we have not yet understood. This would explain why the optical light curve shows no shallow phase-II segment or a break from phase-II to phase-III. What kind of high energy emission do we then expect? In the absence of a real model, we cannot say anything definite. It is possible that the high energy light curve would follow the predictions of the standard model. Perhaps the high energy emission may even be enhanced because the missing X-ray emission is radiated in this band. These are pure speculations, but they are worth keeping in mind. It is very important to carry out high energy observations of GRB afterglows, independent of model expectations, because the signal may in the end turn out to be stronger than anything predicted.

⁸ GeV flat segments followed by a sudden drop are also expected to accompany the X-ray plateaus detected in GRB 060607A (Molinari et al. 2007; Jin & Fan 2007) and GRB 070110 (Troja et al. 2007).

⁹ Interesting EIC emission accompanying Phase-I is also expected.

ACKNOWLEDGMENTS

We thank the second referee for detailed comments. YZF thanks X. Y. Wang and Z. Li for discussions. This work is supported by US-Israel BSF. TP acknowledges the support of Schwartzmann University Chair. YZF and DMW are also supported by the National Science Foundation (grant 10673034) of China and by a special grant of Chinese Academy of Sciences.

REFERENCES

- Aharonian F. A., Atoyan A. M., 1981, *Ap&SS*, 79, 321
 Akerlof C., et al. 1999, *Nature*, 398, 400
 Albert J. et al., 2007, *ApJ*, 667, 358
 Band D., et al. 1993, *ApJ*, 413, 281
 Beloborodov A. M., 2005, *ApJ*, 618, L13
 Blandford, R. D., & McKee, C. F. 1976, *Phys. Fluids.*, 19, 1130
 Blumenthal G. R., Gould R. J., 1970, *Rev. Mod. Phys.*, 42, 237
 Brunetti G., 2001, *Astroparticle Phys.*, 13, 107
 Burrows D. N., et al., 2005, *Science*, 309, 1833
 Chevalier R. A., Li Z. Y., 2000, *ApJ*, 536, 195
 Chincarini G., et al., 2007, *ApJ*, submitted (astro-ph/0702371)
 Cohen, E., Piran, T., 1999, *ApJ*, 518, 346
 Connaughton V., 2002, *ApJ*, 567, 1028
 Cusumano G. et al. , 2007, *A&A*, 462, 73
 Dai Z. G., 2004, *ApJ*, 606, 1000
 Dai Z. G., Gou L. J., 2001, *ApJ*, 552, 72
 Dai Z. G., Lu T., 1998a, *A&A*, 333, L87
 Dai Z. G., Lu T., 1998b, *MNRAS*, 298, 87
 Dai, Z. G., Wang, X. Y., Wu, X. F., Zhang, B., 2006, *Science*, 311, 1127
 Dermer C. D., Chiang J., Mitman K. E. 2000, *ApJ*, 537, 785
 Falcone A. D., et al. 2006, *ApJ*, 641, 1010
 Fan Y. Z., Piran T., 2006a, *MNRAS*, 369, 197
 Fan Y. Z., Piran T., 2006b, *MNRAS*, 370, L24
 Fan Y. Z., Wei D. M., 2005, *MNRAS*, 364, L42
 Fan Y. Z., Xu D., 2006, *MNRAS*, 372, L19
 Fan Y. Z., Zhang B., Proga D., 2005a, *ApJ*, 635, L129
 Fan Y. Z., Zhang B., Wei D. M., 2005b, *ApJ*, 629, 334
 Fenimore E. E., Madras C. D., Nayakshin S., 1996, *ApJ*, 473, 998
 Freedman D. L., Waxman E. 2001, *ApJ*, 547, 922
 Galli A., Piro L., 2006, *A&A*, 455, 413
 Galli A., Piro L., 2007, *A&A*, 475, 421
 Gao W. H., Fan Y. Z., 2006, *Chin. J. Astron. Astrophys.*, 6, 513
 Ghisellini G., George I. M., Fabian A. C., Done C, 1991, *MNRAS*, 248, 14
 Goad M. R., et al., 2006, *A&A*, 449, 89
 González M. M., et al., 2003, *Nature*, 424, 749
 Gou L. J., Mészáros P., 2007, *ApJ*, 668, 392
 Granot J., Guetta D., 2003, *ApJ*, 598, L11
 Granot J., Kumar P., 2006, *MNRAS*, 366, L13
 Granot J., Königl A., Piran T. 2006, *MNRAS*, 370, 1946
 Granot J., Piran, T., Sari, R., 1999, *ApJ*, 513, 679
 Guetta, D. et al., 2007, *A&A*, 461, 95
 Gupta N., & Zhang B., 2007, *MNRAS*, 380, 78
 Horan D., et al., 2007, *ApJ*, 655, 396
 Huang K. Y., et al. 2007, *ApJ*, 654, L25
 Huang Y. F., Gou L. J., Dai Z. G., Lu T., 2000, *ApJ*, 543, 90
 Hurley K., et al., 1994, *Nature*, 372, 652
 in't Zand J. J. M., Heise J., Kippen R. M., Woods, P. M., Guidorzi, C., Montanari E., Frontera F., 2004, *ASPC*, 312, 181
 Ioka K., Toma K., Yamazaki R., Nakamura T. 2006, *A&A*, 458, 7
 Jin Z. P., Fan Y. Z., 2007, *MNRAS*, 378, 1043

- Jones F. C., 1968, *Phys. Rev.*, 167, 1159
- Katz J. I., 1994, *ApJ*, 432, L27
- King A., O'Brien P. T., Goad M. R., Osborne J., Olsson E., Page K., 2005, *ApJ*, 630, L113
- Kobayashi S., Zhang B., Mészáros P., Burrows D. N., 2007, *ApJ*, 655, 391
- Krimm H. A., et al. 2007, *ApJ*, 665, 554
- Kumar P. 2000, *ApJ*, 538, L125
- Kumar P., Panaitescu A., 2000, *ApJ*, 541, L51
- Kumar P., Piran T., 2000, *ApJ*, 532, 286
- Lazzati D., & Perna R., 2007, *MNRAS*, 375, L46
- Liang E. W. et al. , 2006, *ApJ*, 646, 351
- MacFadyen A. I., Woosley S. E., Heger A., 2001, *ApJ*, 550, 410
- Mészáros, P., 2006, *Rep. Prog. Phys.*, 69, 2259
- Mészáros P., Rees M. J., 1994, *MNRAS*, 269, L41
- Mészáros P., Rees M. J., 1999, *MNRAS*, 306, L39
- Mészáros P., Rees M. J., Wijers R. A. M. J., 1998, *ApJ*, 499, 301
- Moderski R., Sikora m., Bulik T., 2000, *ApJ*, 529, 151
- Molinari E., et al., 2007, *A&A*, 469, L13
- Nikoshov A. I., 1962, *Sov. Phys.-JETP*, 14, 393
- Nousek J. A., et al., 2006, *ApJ*, 642, 389
- O'Brien P. T., et al., 2006, *ApJ*, 647, 1213
- Panaitescu, A. et al., 2006, *MNRAS* 369, 2059
- Panaitescu A., Kumar P., 2002, *ApJ*, 571, 779
- Pe'er A., Waxman E., 2004, *ApJ*, 603, L1
- Pe'er A., Waxman E., 2005, *ApJ*, 633, 1018
- Perna R., Armitage P.J., Zhang B., 2006, *ApJ*, 636, L29
- Plaga R., 1995, *Nature*, 374, 430
- Pilla R. P., Loeb A., 1998, *ApJ*, 494, L167
- Piran T., 1999, *Phys. Rep.*, 314, 575
- Piran T., 2004, *Rev. Mod. Phys.*, 76, 1143
- Piran T., Fan Y. Z., 2007, *Phil. Trans. R. Soc. A.*, 365, 1151
- Piro L., et al., 2005, *ApJ*, 623, 314
- Preece R. D., Briggs M. S., Mallozzi R. S., Pendleton G. N., Paciesas W. S., 2000, *ApJS*, 126, 19
- Primack J. R., Bullock, J. S., Somerville, R. S., 2005, *AIPC*, 75, 23
- Proga D., Zhang B., 2006, *MNRAS*, 370, L61
- Rees M. J. 1966, *Nature*, 211, 468
- Rees M. J., Mészáros P., 1998, *ApJ*, 496, L1
- Romano P. et al., 2006, *A&A*, 450, 59
- Rybicki G. B., Lightman A. P., *Radiative Processes in Astrophysics* (Wiley, New York. 1979)
- Sari R., 1998, *ApJ*, 494, L49
- Sari R., Esin A. A., 2001, *ApJ*, 548, 787
- Sari, R., Mészáros, P., 2000, *ApJ*, 535, L33
- Sari R., Narayan R., Piran T., 1996, *ApJ*, 473, 204
- Sari R., Piran T., 1999, *ApJ*, 517, L109
- Sari R., Piran T., Narayan R. 1998, *ApJ*, 497, L17
- Schaefer B. E., et al. 1998, *ApJ*, 492, 696
- Schneid E. J., et al., 1992, *A&A*, 255, L13
- Sommer M., et al., 1994, *ApJ*, 422, L63
- Svensson R., 1987, *MNRAS*, 227, 403
- Takagi R., Kobayashi S., 2005, *ApJ*, 622, L25
- Troja E. et al. , 2007, *ApJ*, 665, 599
- Totani T, 1998, *ApJ*, 502, L13
- Wang X. Y., Dai Z. G., Lu, T., 2001, *ApJ*, 546, L33
- Wang X. Y., Dai Z. G., Lu, T., 2001, *ApJ*, 556, 1010
- Wang X. Y., Li Z., Mészáros P., 2006, *ApJ*, 641, L89
- Wang X. Y., Mészáros P., 2006, *ApJ*, 643, L95
- Waston D., et al., 2006, *ApJ*, 637, L69
- Waxman E., 1997, *ApJ*, 491, L19
- Wei D. M., Cheng K. S., 1997, *MNRAS*, 290, 107
- Wei D. M., Fan Y. Z., 2007, *Chin. J. Astron. Astrophys.*, 7, 509
- Wei D. M., Yan T., Fan Y. Z., 2006, *ApJ*, 636, L69
- Weiler, K. W., Panagia, N., Montes, M. J., SramekWei, R. A. 2002, *ARA&A*, 40, 387
- Wu X. F., Dai Z. G., Wang X. Y., Huang Y. F., Feng L. L., Lu T., 2006, *ApJ*, submitted (astro-ph/0512555)
- Xue R. R., et al. 2008, *ApJ*, to be submitted
- Yost S., Harrison F. A., Sari R., Frail D. A., 2003, *ApJ*, 597, 459
- Yu, Y. W., Liu, X. W., & Dai, Z. G., 2007, *ApJ*, in press (arXiv: astro-ph/07063741)
- Zhang B., 2007, *Chin. J. Astron. Astrophys.*, 7, 1 (astro-ph/0701520)
- Zhang B., Fan Y. Z., Dyks J., Kobayashi S., Mészáros P., Burrows D. N., Nousek J. A., Gehrels N. 2006, *ApJ*, 642, 354
- Zhang B., Mészáros P., 2001a, *ApJ*, 552, L35
- Zhang B., Mészáros P., 2001b, *ApJ*, 559, 110
- Zhang W. Q., Woosley S. E., Heger A., 2007, *ApJ*, in press (astro-ph/0701083)
- Zou Y. C., Dai Z. G., Xu, D., 2006, *ApJ*, 646, 1098